Turbid: A **turb**ulence-resolving numerical model for simulating bottom boundary layer and f**i**ne se**d**iment transport

by

Liangyi Yue[a], Zhen Cheng[b,c], Tian-Jian Hsu[a]

[a] *Center for Applied Coastal Research, Civil and Environmental Engineering, University of Delaware, Newark, DE 19716, USA*
[b] *Applied Ocean Physics and Engineering, Woods Hole Oceanographic Institution, Woods Hole, MA 02543, USA*
[c] *Convergent Science, Inc., Madison, WI 53719, USA*

Research Report **NO. CACR-19-02**

Center For Applied Coastal Research
University of Delaware
Newark, DE 19716, USA

April 9, 2019

Acknowledgements

This study is supported by NSF (OCE-1537231) and Office of Naval Research (N00014-17-1-2796). Numerical simulations presented in this report were carried out using the Mills and Canviness clusters at University of Delaware, and the SuperMIC cluster at Louisiana State University via XSEDE (TG-OCE100015).

Abstract

Turbulent bottom boundary layer with possible fine sediment transport is particularly of interest for the coastal and oceanographic community, where the turbulence-resolving numerical simulations can be applied to reveal fundamental mechanism behind the flow dynamics. Benefit from the significant advances in computer science in recent years, a novel and scalable numerical modeling system for turbulence-resolving numerical simulation of multiphase flow is built and introduced in this report. Model formulation of the numerical system follows the classical theory for the 3D incompressible Navier-Stokes equations and pseudo-spectral numerical method, which has been widely used by many other studies. A two-level parallelization strategy is applied in the system for stable computation performance and reliable scalability. Through the study of three different kinds of boundary layer flows, the numerical modeling system is rigorously benchmarked after the comparison with analytical solution, turbulence-model based theory, and corresponding direct numerical simulation results reported by other studies. Through these simulations, the newly built system demonstrates its capability in simulating bottom boundary layer flows with fine sediment transport. Other features, such as the bedforms and multi-class sediment, are planned to be integrated in this modeling system making it capable of simulating flow in more realistic situations.

Contents

List of Figures

1. Introduction

The technique of direct numerical simulation (DNS) has been widely used to investigate turbulent flows, in which the 3D Navier-Stokes equations are numerically solved without any turbulence model. DNS aims at obtaining high accuracy numerical solution such that the whole range of spatial and temporal scales of turbulence and the entire energy cascade process from the energy containing scale down to the Kolmogorov scale are fully resolved (Kim et al. (1987)). In the past two decades, DNS has also been wide used to study fine particle transport in turbulent flow. Since the particle phase in most of these studies are treated as a continuum while the particle sizes are smaller than the Kolmogorov length scale, the energy cascade processes can still be well-resolved. Nevertheless, we shall call such simulation methodology simply as turbulence-resolving numerical simulation (TRNS). In the past decade, the DNS or TRNS demonstrates its advantage in studying many geophysical flow problems (Nelson and Fringer (2018); Remmler et al. (2013); Xu et al. (2016); Zhao et al. (2018)). Although the Reynolds number achieved by these studies remains to be orders of magnitude lower than the field condition, significant insights on fundamental dynamics have been revealed to advance our understanding of these complex phenomena.

In this report, the turbulence-resolving numerical simulation based on the pseudo-spectral scheme (Canuto et al. (1988); Peyret (2002)) of the two-way coupled particle-laden flow is of our interest. This type of modeling framework has been extensively used in studying self-sustaining turbidity currents (Cantero et al. (2009a,b, 2014); Shringarpure et al. (2012)). We are particularly interested in fine sediment transport in the wave bottom boundary layer over gentle slopes which further relies on the wave-induced fluid turbulence as the main suspension mechanism. Thus, key processes of interest here may be fundamentally different from the turbidity current which is sustained by the forward motion of the current itself (Meiburg and Kneller (2010); Parker et al. (1986)). For such wave-driven fine sediment transport, the TRNSs have been

used by the previous studies (Cheng et al. (2015b); Ozdemir et al. (2010)) to investigate the sediment-induced attenuation effect on flow turbulence and the resulting sediment transport modes that may lead to the understanding of the dynamics of wave-supported gravity flows (WSGFs). WSGF is a type of density (gravity) current driven by sediment-induced buoyancy effect taking place in the thin wave bottom boundary layer usually observed on continental shelves (Hale and Ogston (2015); Traykovski et al. (2000, 2007)). Its dynamics are further controlled by sediment-induced attenuation of flow turbulence in the low to intermediate Reynolds number in transitionally turbulent regime (Thorpe (1987)). This is a remarkable geophysical problem as the Reynolds number is attainable by DNS/TRNS using the existing computational resources. Moreover, due to the high sediment concentration within the thin wave bottom boundary layer, it is highly challenging to measure detailed flow velocity, sediment concentration and turbulence statistics in laboratory or field (Trowbridge and Lentz (2018)). Therefore, DNS becomes an unique tool to gain insights of the wave boundary layer turbulence and flow-sediment interaction at a Reynolds number similar to that in the field condition. However, existing studies do not directly simulate the event-scale WSGFs which either require simulation of several tens to hundreds of wave periods, or do not include complex bathymetry, such as small bedforms. Bedforms have been observed in WSGF events in the field (Traykovski et al. (2015)) and are shown in the laboratory experiments to be possibly caused by a small fraction of very fine sand in the mud (Hooshmand et al. (2015)). Hooshmand et al. (2015) further suggest that the presence of bedforms can enhance turbulence in the wave bottom boundary layer which counteract with the turbulence-damping effects due to the sediment-induced density stratification.

Equipped with these understandings, there are three steps in our numerical model development. Firstly, we like to build a highly scalable numerical framework for turbulence-resolving simulation of bottom boundary layer flow and fine sediment transport, allowing the usage of hundreds to thousands of CPUs in distributed memory system. The resulting numerical modeling system will allow us to carry out simulations of bottom boundary layer processes at

high Reynolds number for event-scale analysis. Secondly, with such a scalable numerical framework, the coordinate transformation (Ge et al. (2010); Yang and Shen (2011)) will be applied in the modeling system such that we can expand our simulation study for flow over complex bathymetry. Finally, the framework will be extended for other capabilities, such as multi-class sediment transport (Shringarpure et al. (2014)). The final goal is to develop a numerical modeling system which is capable of turbulence-resolving simulations of fine sediment transport in a more realistic bottom boundary layer.

This report documents model formulation and detailed numerical implementation serving as the first step of the model development, namely the numerical modeling framework for single class fine sediment transport over a flat bottom. The numerical model is written in object-oriented `C++` programming language. The Message Passing Interface (MPI) with a 2D pencil decomposition of computational domain is used for parallel computing (Pekurovsky (2012)). Other numerical treatments in the pseudo-spectral method are similar to that reported in Cortese and Balachandar (1995); Ozdemir et al. (2010) and Cheng et al. (2015b). The numerical modeling system is further used to simulate several benchmark problems to verify its scalability and capability.

The remaining of this report is organized as follows. A description of model formulation for fluid flow and fine sediment transport is given in Chapter 2. The numerical implementation of the proposed mathematical formulation is discussed in detail in Chapter 3. Three types of benchmark simulation are presented in Chapter 4 to verify the numerical model and to demonstrate the model applications. This report is concluded in Chapter 5 along with a discussion on future model development.

2. Model Formulation

2.1. Problem Setup and Computational Domain

As stated in Section 1, our goal is to develop a high numerical accuracy and scalable numerical model for turbulence-resolving simulation of bottom bound-

ary layer and fine sediment transport processes. Due to the transitional nature of coastal wave bottom boundary layer and turbulence attenuation by the presence of sediments, the turbulence-resolving simulation technique may be advantageous over the conventional and more widely-used Reynolds-averaged models. Particularly for coastal and oceanographic community, turbulence-resolving models can serve as a useful tool to isolate various mechanisms in determining the resulting complex and coupled processes associated with transitional turbulent flow and sediment transport. Focusing on simulating the near-bed fluid dynamics, an idealized computational domain (Figure 1) covering the bottom boundary layer is established. In a coordinate system with its origin defined at a bottom corner, the rectangular domain has a size of $L_1 \times L_2 \times L_3$ in the streamwise (x_1), the spanwise (x_2), and the vertical (x_3) direction, respectively.

For the numerical simulations presented in this report, the domain can have a free-slip surface to avoid undesired effects from the treatment of top boundary on the bottom boundary layer. In contrast, the bottom of domain is regarded as a no-slip flat wall for the boundary layer flow. When fine sediment transport is simulated in the domain (see the schematic plot shown in Figure 1), the bottom

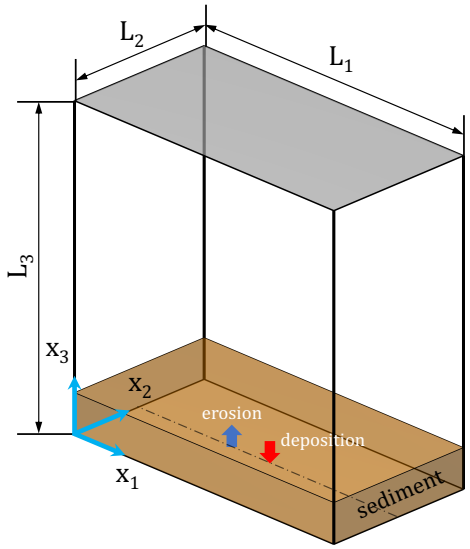

Figure 1. Sketch of computational domain and definition of coordinate system.

can be treated as an erodible bed for the sediment phase where the processes of sediment exchange with the bed are modeled based on local bottom shear stress and sediment concentration. In this report, the erodible bed is assumed to be made up of uniform fine sediments. Following Ozdemir et al. (2010), a constant settling velocity of w^* is specified and the flocculation process of fine sediment (Soulsby et al. (2013)) is ignored. As a result, the sediments in suspension are idealized as monodispersed and assumed to be of a given diameter with a submerged specific gravity of $R = 1.65$. For simplicity, all the benchmark applications to be discussed in Section 4 are assumed to consist of silt sized sediment of diameter 24 µm and the resulting settling velocity is specified as $w^* = 0.5\,\mathrm{mm/s}$. In the two horizontal (x_1 and x_2) directions, periodic boundary conditions are implemented by assuming that the resultant flow is statistically homogeneous in these two directions.

2.2. Governing Equations and Boundary Conditions

The model formulation is introduced in this section using dimensionless variables which are nondimensionlized with a characteristic velocity scale U^*, a length scale H^*, and the corresponding time scale H^*/U^*. For different applications presented in Section 4, these scales will be determined accordingly. At this moment, we also would like to point out that in this report, a variable with superscript symbol '*' is dimensional except for general physical constants, such as the fluid kinematic viscosity ν, the gravitational acceleration constant g, and the water density ρ.

2.2.1. The Two-Phase Flow Eulerian Method

In this study, the widely used equilibrium Eulerian approach (Balachandar and Eaton (2010)) is applied for simulations of fine sediment transport in the bottom boundary layer. Under the assumption that the inertia of suspended fine sediment particles in water is very small, the suspended sediments can follow the local carrier flow closely (Ferry and Balachandar (2001); Ferry et al. (2003)). In terms of the nondimensional parameter, this requires the Stokes number (defined

here as the ratio of the particle response time to the Kolmogorov time scale) to be smaller than 0.3 (Cantero et al. (2008)). The validity of applying this approximation to fine sediment transport in wave bottom boundary layer has been discussed in Cheng et al. (2015a) and hence we adopt the same assumption in this study. Consequently, the velocity field of sediment phase v_i can be determined from the velocity field of carrier flow u_i and the particle settling velocity w as

$$v_i = u_i + w n_i, \tag{1}$$

where n_i denotes the ith direction component of the gravitational acceleration vector. For clarity, tensor notation is utilized hereafter and the subscript $i = 1, 2, 3$ corresponds to the streamwise x_1, spanwise x_2 and vertical direction x_3, respectively. The application of the equilibrium Eulerian approach results in the fast Eulerian method for two-phase flow problems. By avoiding solving particle momentum equations and the corresponding coupling processes (Ferry et al. (2003)), this approach distinguishes itself from the full Eulerian two-phase flow formulation for its simplicity and thus it is more straightforward to be solved by a pseudo-spectral scheme.

2.2.2. Fluid Dynamic Solver

For dilute fine sediment transport in water, we apply the Boussinesq approximation to further simplify the governing equations for the carrier flow phase. Subject to the continuity equation $\partial u_i/\partial x_i = 0$, the incompressible Navier-Stokes momentum equations for carrier flow read (Shringarpure et al. (2012))

$$\frac{\partial u_i}{\partial t} + u_j \frac{\partial u_i}{\partial x_j} = -\frac{\partial p}{\partial x_i} + \frac{1}{\mathrm{Re}} \frac{\partial^2 u_i}{\partial x_j \partial x_j} + \frac{1}{\mathrm{Fr}^2} \phi n_i + S_i, \tag{2}$$

where $\mathrm{Fr} = U^*/\sqrt{RgH^*}$ is the particle Froude number. Here, p is the dynamic pressure of fluid phase and ϕ denotes the volumetric concentration of sediment. In Equation (2), the buoyancy (3^{rd} term on the right-hand-side) term accounts the coupling-effects from sediment phase, which vanishes for clear flow simulations. The source (last) term represents the flow forcing, which is applied via a prescribed pressure gradient for the generation of specific flows, e.g. currents

and/or waves. As shown in Section 4, the computed sediment volumetric concentration in this study is less than 0.05 and thus the simplified Equation (2) is applicable (Cheng et al. (2015b)).

The bottom of the computational domain is modeled as an erodible bed when sediments present (or a solid wall for clear flow) and the no-slip boundary condition is applied for the carrier flow phase which can be written as

$$u_i = 0 \qquad \text{at} \quad x_3 = 0. \tag{3}$$

In contrast, two different types of boundary condition are available on top of the computational domain. For simulations of channel flow, the no-slip boundary condition $u_i = 0$ at $x_3 = L_3$ should be implemented. However, in many bottom boundary layer problems, the computational domain can be better modeled as a shear-free top boundary where the free-slip, rigid-lid boundary condition is implemented

$$\frac{\partial u_1}{\partial x_3} = 0, \ \frac{\partial u_2}{\partial x_3} = 0, \ u_3 = 0 \qquad \text{at } x_3 = L_3. \tag{4}$$

2.2.3. Sediment Transport Solver

Derived from the principle of mass conservation, the resulting advection-diffusion equation for the volumetric concentration of sediment is written as (Shringarpure et al. (2012))

$$\frac{\partial \phi}{\partial t} + \frac{\partial \left(\phi v_j\right)}{\partial x_j} = \frac{1}{\mathrm{ReSc}} \frac{\partial^2 \phi}{\partial x_j \partial x_j}, \tag{5}$$

where $\mathrm{Sc} = \nu / K$ is the Schmidt number, and K is the effective diffusivity of sediment. Following the previous studies (Ozdemir et al. (2010); Cheng et al. (2015b)), the Schmidt number is specified as a constant value of 0.5 in this study.

For sediment phase, the no-flux boundary condition is applied at the top of computational domain. This condition imposes no net transport of sediment across the top boundary throughout computation which reads (Ozdemir et al. (2010))

$$v_3 \phi - \frac{1}{\mathrm{ReSc}} \frac{\partial \phi}{\partial x_3} = 0 \qquad \text{at } x_3 = L_3. \tag{6}$$

At the bottom of computational domain, the no-flux boundary condition can be applied such that the total amount of sediment is specified by the initial condition, which can further be quantified by the bulk Richardson number (Ozdemir et al. (2010)). In addition, the erodible/depositional boundary condition (Cheng et al. (2015b)) is available in this model framework for modeling more realistic sediment exchange process, which allows for sediment entrainment/deposition from/to the bed. Following the expression of Equation (6), this condition is written as

$$v_3\phi - \frac{1}{\mathrm{ReSc}}\frac{\partial\phi}{\partial x_3} = q_e + q_d \qquad \text{at } x_3 = 0, \tag{7}$$

where q_e and q_d are the erosional and depositional fluxes at the bottom, respectively. Following the continuous deposition formulation (Sanford (2008)), the depositional flux is modeled as $q_d = \phi w n_3$. The erosional flux is calculated using the Partheniades-Ariathurai-type formulation (Sanford and Maa (2001); Winterwerp et al. (2012)) which has the following nondimensional expression

$$q_e = \begin{cases} m_e\left(\dfrac{|\tau_b|}{\tau_c} - 1\right) & \text{for } |\tau_b| \geq \tau_c \\ 0 & \text{for } |\tau_b| < \tau_c \end{cases}, \tag{8}$$

where τ_c is the (dimensionless) critical bottom shear stress of erosion, τ_b is the bottom shear stress and $|\tau_b|$ denotes its magnitude. According to Equation (8), the erosional flux is adjusted by the value of $|\tau_b|$ which is a function of time and space. For simulations reaching a statistical equilibrium state, we expect the depositional flux balances the erosional flux from the time-averaging perspective and the corresponding time-averaged depth-integrated sediment in computational domain becomes temporally invariant.

2.3. Variable Decomposition and Notation

Various averaging procedures are summarized in this section, which will be used in later section for data analysis. We consider the most general situation where the bottom boundary layer is driven by waves with a concurrently superimposed mean current. The resulting wave-current interaction makes the

data analysis difficult, and thus the triple decomposition method is used to isolate the organized variations in the fluctuating field of turbulent flow (Baj et al. (2015); Kwon et al. (2016)). By using this method, the fluctuating field is decomposed into current, wave and fluctuation components. This kind of decomposition is also applicable for flow with pure current or waves only. In the triple decomposition, the time and phase-averaged components of an arbitrary fluctuating quantity $\psi\left(x_1, x_2, x_3; t\right)$ are respectively defined as (Reynolds and Hussain (1972))

$$\overline{\psi} = \frac{1}{MT_w} \int_{M_1 T_w}^{M_2 T_w} \psi\left(x_1, x_2, x_3; t\right) dt, \tag{9}$$

$$\langle \psi \rangle_p = \frac{1}{M} \sum_{n=0}^{M-1} \psi\left(x_1, x_2, x_3; t + nT_w\right), \tag{10}$$

where $M = M_2 - M_1$ is the number of wave periods in time interval $\begin{bmatrix} M_1 T_w & M_2 T_w \end{bmatrix}$ during which the data analysis is taken. Corresponding to the definition of time average, the averaging operation over space is written as

$$\langle \psi \rangle_i = \frac{1}{L_i} \int_0^{L_i} \psi\left(x_1, x_2, x_3; t\right) dx_i. \tag{11}$$

Note that the average operations defined in Equations (9) and (11) are commutative. As a result, the combination of multiple average operations can be denoted by the subscripts of the average operator '$\langle\,\rangle$', except for the time average. Accordingly, for an arbitrary variable ψ, the expression $\langle \psi \rangle_{123}$ represents its domain-averaging while $\langle \psi \rangle_{p12}$ represents its phase- and plane-averaging.

Consequently, we apply a triple decomposition for current-wave-turbulence decomposition similar to the one proposed in Nelson and Fringer (2018). We decompose a variable ψ into a current component $\langle \psi \rangle_c$, a wave component $\langle \psi \rangle_w$, and a fluctuating component ψ' as

$$\psi = \langle \psi \rangle_c \left(x_3\right) + \langle \psi \rangle_w \left(x_3; t\right) + \psi'\left(x_1, x_2, x_3; t\right). \tag{12}$$

In this expression, each component is defined as follows

$$\langle\psi\rangle_c = \langle\overline{\psi}\rangle_{12}, \tag{13}$$

$$\langle\psi\rangle_w = \langle\psi\rangle_{p12} - \langle\psi\rangle_c, \tag{14}$$

$$\psi' = \psi - \langle\psi\rangle_c - \langle\psi\rangle_w = \psi - \langle\psi\rangle_{p12}. \tag{15}$$

In other words, we approximate the current component of a variable $\langle\psi\rangle_c$ by the time- and plane-averaging of the simulation results, namely $\langle\overline{\psi}\rangle_{12}$. The wave component $\langle\psi\rangle_w$ is then extracted by subtracting the current component $\langle\psi\rangle_c$ from the phase- and plane-averaged quantity $\langle\psi\rangle_{p12}$. After obtaining the wave and current components, the turbulent fluctuating component ψ' can be computed accordingly.

3. Numerical Implementation

A novel numerical modeling system is built based on the theoretical formulation described in Sections 2.2.2 and 2.2.3. Pseudo-spectral method is used to solve the governing equations with corresponding boundary conditions, which follows the pioneering work of Cortese and Balachandar (1995). Detailed numerical discretization in time and space are respectively introduced in Section 3.1 and Section 3.2. The numerical solution procedure is summarized in Section 3.3.

3.1. Time Integration and Boundary Treatment

The equation system (Equations (2) and (5)) is advanced in time by a third-order low-storage Runge-Kutta scheme (Williamson (1980)) where the Courant-Friedrichs-Lewy (CFL) condition is implemented to limit the size of time step by specifying a maximum Courant number. With application of the equilibrium Eulerian approach (see Section 2.2.1), the carrier flow and fine sediment phases are solved separately and consecutively in one time step.

3.1.1. The Two-Stage Projection Method

The momentum Equation (2) of the carrier flow phase is numerically solved following Chorin's projection method (Chorin (1968)). During each of the three

time levels of a computational step in the third-order Runge-Kutta scheme, the standard two-stage projection is utilized to enforce a divergence-free velocity field of the carrier flow. In the predictor stage, an intermediate velocity $u_i^\star$ is first computed explicitly using the momentum equation by ignoring the pressure gradient term

$$\frac{\partial^2 u_i^{(m\star)}}{\partial x_j \partial x_j} - \frac{\mathrm{Re}}{\Delta t c_3\,(m)} u_i^{(m\star)} = -\frac{\mathrm{Re}}{\Delta t c_3\,(m)} \left[u_i^{(m-1)} + c_2\,(m)\, h_i^{(m)} \right] - \frac{\partial^2 u_i^{(m-1)}}{\partial x_j \partial x_j}, \tag{16}$$

where index $m = \begin{bmatrix} 1 & 2 & 3 \end{bmatrix}$ indicates the three time levels in a time step Δt, and the semi-implicit second-order Crank-Nicolson method is implemented for the diffusion term to relax the strong stability restriction of time step. In Equation (16), the temporary variable h_i has an expression written as

$$h_i^{(m)} = \Delta t \left[S_i + \frac{1}{\mathrm{Fr}^2} \phi^{(m-1)} n_i - A\left(u_i^{(m-1)}, u_j^{(m-1)} \right) \right] + c_1\,(m)\, h_i^{(m-1)}, \tag{17}$$

where $A(\bullet)$ denotes the advection operator in which the Arakawa scheme (Arakawa and Lamb (1981)) is used. Moreover, the classical 3/2 rule is implemented in the advection operator to remove aliasing error (Peyret (2002)). Arising from the above equations, the three coefficients are $c_1 = \begin{bmatrix} 0 & -\frac{5}{9} & -\frac{153}{128} \end{bmatrix}$, $c_2 = \begin{bmatrix} \frac{1}{3} & \frac{15}{16} & \frac{8}{15} \end{bmatrix}$, and $c_3 = \begin{bmatrix} \frac{1}{6} & \frac{5}{24} & \frac{1}{8} \end{bmatrix}$. Notice that Equation (16) is now cast in form of the Helmholtz equation and it will be solved with the procedure to be discussed in Section 3.2.1. In the corrector stage, the intermediate velocity is corrected with pressure gradient in order to obtain the final solution of the time level u_i as

$$u_i^{(m)} = u_i^{(m\star)} - 2\Delta t c_3\,(m) \frac{\partial p^{(m)}}{\partial x_i}, \tag{18}$$

where the dynamic pressure p is computed by solving the Poisson's equation with Neumann boundary condition $\partial p^{(m)}/\partial x_3 = 0$ at $x_3 = \pm 1$ in vertical direction, which is written as

$$\frac{\partial^2 p^{(m)}}{\partial x_j \partial x_j} = \frac{1}{2\Delta t c_3\,(m)} \frac{\partial u_j^{(m\star)}}{\partial x_j}. \tag{19}$$

This equation is further solved with a direct method to be discussed in Section 3.2.

Respectively, boundary conditions of the intermediate velocity and dynamic pressure are still required for solving Equation (16), which are based on the linear extrapolation of the dynamic pressure gradient, which reads

$$\frac{\partial p^{(m)}}{\partial x_i} = \left[1 + c_4\left(m\right)\right] \frac{\partial p^{(m-1)}}{\partial x_i} - c_4\left(m\right) \frac{\partial p^{(m-2)}}{\partial x_i} + O\left(\Delta t^2\right), \tag{20}$$

where $c_4\left(m\right) = c_3\left(m\right)/c_3\left(m-1\right)$ and $c_3\left(0\right) = c_3\left(3\right)$. When $m = 1$, Equation (20) has the dynamic pressure gradient $\partial p^{(-1)}/\partial x_i$, which refers to the computed value in second time level ($m = 2$) of the last time step. From Equation (18) with $u_i^{(m)} = 0$, the no-slip boundary condition for the intermediate velocity can be expressed as

$$u_i^{(m\star)} = 2\Delta t c_3\left(m\right) \left\{ \left[1 + c_4\left(m\right)\right] \frac{\partial p^{(m-1)}}{\partial x_i} - c_4\left(m\right) \frac{\partial p^{(m-2)}}{\partial x_i} \right\}, \tag{21}$$

where high-order terms of Δt are neglected. For simulation with a free-slip boundary on top of the computational domain, the partial derivative with respect to x_3 on both sides of Equations (18) and (20) is taken and after some algebraic manipulation, the corresponding top boundary condition for the intermediate velocity reads

$$\frac{\partial u_i^{(m\star)}}{\partial x_3} = 2\Delta t c_3\left(m\right) \left\{ \left[1 + c_4\left(m\right)\right] \frac{\partial^2 p^{(m-1)}}{\partial x_i \partial x_3} - c_4\left(m\right) \frac{\partial^2 p^{(m-2)}}{\partial x_i \partial x_3} \right\}, \tag{22}$$

where $i = 1, 2$ for the two horizontal directions only. In vertical direction, the free-slip boundary condition requires $u_3^{(m)} = 0$ and the same condition as Equation (21) but at $x_3 = 1$ is applied.

3.1.2. Solution of Scalar Transport in Flow

Right after the velocity-projection procedure for the carrier flow phase (see Section 3.1.1) is solved, the sediment concentration is computed by solving Equation (5) with the boundary conditions (6) and (7) using a procedure similar to the predictor stage of carrier flow (Equation (16)). This discretized advection-diffusion equation is written as

$$\frac{\partial^2 \phi^{(m)}}{\partial x_j \partial x_j} - \frac{\mathrm{ReSc}}{\Delta t c_3\left(m\right)} \phi^{(m)} = -\frac{\mathrm{ReSc}}{\Delta t c_3\left(m\right)} \left[\phi^{(m-1)} + c_2\left(m\right) h_s^{(m)}\right] - \frac{\partial^2 \phi^{(m-1)}}{\partial x_j \partial x_j}, \tag{23}$$

where the temporary variable h_s has the following expression

$$h_s^{(m)} = \Delta t \left[-A\left(v_i^{(m)}, \phi^{(m-1)}\right) \right] + c_1\,(m)\, h_s^{(m-1)}. \tag{24}$$

Equation (23) is written in the form of a Helmholtz equation and it can be solved directly (see Section 3.2.1). From Equation (1), the velocity field of sediment in Equation (24) is updated using the newest computed u_i, as

$$v_i^{(m)} = u_i^{(m)} + wn_i. \tag{25}$$

3.2. Spatial Discretization and Matrix Representation

The Laplace's Equation (19) of dynamic pressure can be regarded as a special case of the more general Helmholtz equation. In fact, along with Equation (16) and Equation (23), these equations introduced in Section 3.1 can be categorized as a set of the Helmholtz equations. Thus, the final issue becomes seeking numerical solution of the resultant Helmholtz equations. For a more concise presentation, the representation based on matrices is used in this section.

3.2.1. The Resulting Helmholtz Equations

The Helmholtz Equations (16), (19) and (23) of the present model system can be rewritten as follows

$$\left[\frac{\partial^2}{\partial x_j \partial x_j} - \mathbf{A}^{(m)} \right] \circ \mathbf{X}^{(m)} = \mathbf{B}^{(m)}, \tag{26}$$

where the operator symbol "$\circ$" denotes the Hadamard (entrywise) product, and the bold symbols denote vectors or matrices which read

$$\mathbf{A}^{(m)} = \frac{1}{\Delta t c_3\,(m)} \begin{bmatrix} \mathrm{Re} \\ 0 \\ \mathrm{ReSc} \end{bmatrix}, \tag{27}$$

$$\mathbf{X}^{(m)} = \begin{bmatrix} u_i^{(m\star)} \\ p^{(m)} \\ \phi^{(m)} \end{bmatrix}, \tag{28}$$

$$\mathbf{B}^{(m)} = \begin{bmatrix} -\dfrac{\mathrm{Re}}{\Delta t c_3\,(m)}\left[u_i^{(m-1)} + c_2\,(m)\,h_i^{(m)}\right] - \dfrac{\partial^2 u_i^{(m-1)}}{\partial x_j \partial x_j} \\ \dfrac{1}{2\Delta t c_3\,(m)}\dfrac{\partial u_j^{(m\star)}}{\partial x_j} \\ -\dfrac{\mathrm{ReSc}}{\Delta t c_3\,(m)}\left[\phi^{(m-1)} + c_2\,(m)\,h_s^{(m)}\right] - \dfrac{\partial^2 \phi^{(m-1)}}{\partial x_j \partial x_j} \end{bmatrix}. \tag{29}$$

As stated in Section 3.1, each element in $\mathbf{X}^{(m)}$ is computed successively following the order u_i, p and to ϕ by solving the corresponding matrix system (Equation (26)). The matrix system is solved by using the Fourier-Chebyshev collocation method to be discussed next while the detailed solution procedure of the numerical framework is summarized in Section 3.3.

3.2.2. The Matrix Multiplication Technique

The Fourier-Chebyshev collocation method (Canuto et al. (1988)) is used to solve the matrix Equation (26), and the computation domain is discretized uniformly in horizontal (streamwise and spanwise) directions but nonuniformly in vertical direction with $N_1 \times N_2 \times N_3$ gird points, respectively. Location of these grid points in computational domain are

$$x_{1j} = \frac{jL_1}{N_1} \qquad \text{with} \;\; 0 \le j \le N_1 - 1, \tag{30}$$

$$x_{2j} = \frac{jL_2}{N_2} \qquad \text{with} \;\; 0 \le j \le N_2 - 1, \tag{31}$$

$$x_{3j} = \cos\left(\frac{j\pi}{N_3}\right) \qquad \text{with} \;\; 0 \le j \le N_3. \tag{32}$$

For the two horizontal directions, the Fourier expansion is implemented to enforce the periodic boundary condition, while the Chebyshev expansion on the Chebyshev-Gauss-Lobatto (CGL) points is utilized in the vertical direction. After the application of the matrix multiplication technique (Peyret (2002)), the governing equation for each element of $\mathbf{X}^{(m)}$ can be represented by a set of linear equations in the wavenumber domain as

$$\left[\mathbf{D}^2 - \left(k_{1\alpha}^2 + k_{2\beta}^2 + a_n(m)\right)\mathbf{I}\right]\hat{\mathbf{x}}_{n\alpha\beta}^{(m)} = \hat{\mathbf{b}}_{n\alpha\beta}^{(m)}, \tag{33}$$

where $\mathbf{D}^2$ denotes the second-order differentiation matrix in vertical direction, and $\mathbf{I}$ denotes the identity matrix. In Equation (33), a_n, $\mathbf{x}_n$ and $\mathbf{b}_n$ are the nth element of $\mathbf{A}$, $\mathbf{X}$ and $\mathbf{B}$, respectively. Variable marked with an overscore symbol "ˆ" is in the wavenumber domain due to the discrete Fourier transform (DFT) in horizontal directions. The subscript α and β indicates the index of Fourier modes which are in range of

$$-N_1/2 \leq \alpha \leq N_1/2 - 1, \tag{34}$$

$$-N_2/2 \leq \beta \leq N_2/2 - 1. \tag{35}$$

Correspondingly, the wavenumbers in the streamwise and spanwise direction are $k_{1\alpha}$ and $k_{2\beta}$. The resulting linear Equation (33) is solved directly by using the matrix-diagonalization method (Peyret (2002)) with the boundary conditions described in Section 3.1.

3.3. Summary of Numerical Solution Procedure

After the time integration (see Section 3.1) and spatial discretization (see Section 3.2), the governing Equations (2) and (5) are represented by the general linear Equation (33). With suitable boundary conditions, the equation system is numerically solved and the solution procedure is summarized as follows

(a) Initialize variable $u_i^{(0)}$, $p^{(0)}$ and $\phi^{(0)}$ with given input or from the last time step; Set the time level counter as $m = 1$.

(b) Update $h_i^{(m)}$ using Equation (17) and $b_1^{(m)}$ using Equation (29); Solve Equation (33) for $u_i^{(m\star)}$ with $n = 1$, and boundary conditions (21) and (22).

(c) Update $b_2^{(m)}$ using Equation (29) with the newly computed $u_i^{(m\star)}$; Solve Equation (33) for $p^{(m)}$ with $n = 2$ and the Neumann boundary condition.

(d) Project $u_i^{(m\star)}$ to $u_i^{(m)}$ using Equation (18); Update the velocity field of fine sediment using Equation (25).

(e) Update $h_s^{(m)}$ using Equation (24) and $b_3^{(m)}$ using Equation (29); Solve Equation (33) for $\phi^{(m)}$ with $n = 3$, and boundary conditions (6) and (7).

(f) If $m < 3$, update the time level counter as $m = m + 1$ and goto Item (b) for the next time level; If $m = 3$, output $u_i = u_i^{(3)}$, $p = p^{(3)}$ and $\phi = \phi^{(3)}$ as the computed results for current time step; Update time step Δt based on a CFL criterion and goto Item (a) for the next circle until meeting a termination criteria of the computation.

Written in `C++` using the object-oriented programming language, the numerical modeling system implements the above solution procedure based on the Message Passing Interface (MPI) technique. For parallelization, the two different levels discussed below have been used in the system and the scalability test (Figure 2) demonstrates a good computation efficiency of present numerical modeling system.

a) *The parallelization between computer nodes.* For such a level of parallelization, the so-called 2D pencil decomposition (Pekurovsky (2012)) of computation domain has been applied through the MPI. The well-known numerical library P3DFFT (Pekurovsky (2012)) is used for the discrete Fourier transform in the two horizontal directions. This procedure of DFT turns out to be the major load of computation.

b) *The parallelization in a local computer node.* Equipped with the user-friendly numerical library Armadillo (Sanderson and Curtin (2016)), the programming process becomes relatively easy. More importantly, the library employs a delayed evaluation approach to combine several operations into one and reduce (or eliminate) the need for temporaries and accelerates a lot of chained operations.

4. Model Application

The numerical model introduced in Section 3 is benchmarked through the study of turbulent boundary layers in several different situations, where the fluid

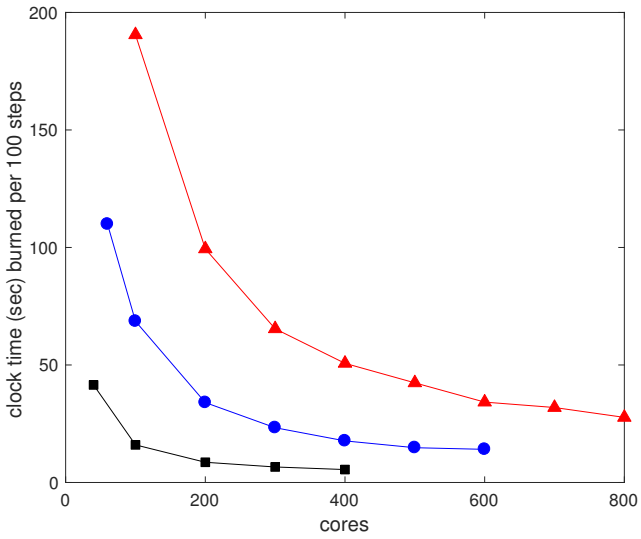

Figure 2. Scalability test result for three runs having different total number of grid points of the present modeling system taken on the LSU (Louisiana State University, USA) supercomputer SuperMIC. The black line marked with squares donates a run of $128 \times 128 \times 129$ grid points, the blue line marked with bullets donates a run of $192 \times 192 \times 193$ grid points, and the red line marked with triangles donates a run of $256 \times 256 \times 257$ grid points.

(Section 2.2.2) and sediment (Section 2.2.3) solvers are verified correspondingly.

4.1. Statistically Steady Channel Flow

Before simulating the turbulent channel flow, it is fundamental to verify the model with the laminar flow condition where the analytical solution is available. Resulting from a sudden application of a spatially constant pressure gradient to a fluid initially at rest, the transient laminar channel flow is such a good example of a time-dependent flow problem amenable to exact mathematical analysis with an analytical solution expressed as (Duarte et al. (2008))

$$u_{1a} = \frac{\mathrm{Re}\left(1 - x_3^2\right)}{2} - 16\mathrm{Re}\sum_{n=1}^{\infty}\left[m^{-3}\sin\frac{m\left(1+x_3\right)}{2}\exp\left(-\frac{m^2 t}{4}\right)\right], \qquad (36)$$

where $m = (2n-1)\,\pi$. For numerical setup, the domain has a size of $4\pi H \times 4\pi H/3 \times 2H$ and $H = 0.5L_3$ is the half channel height. Since the flow is laminar, only two grid points are used in horizontal directions to save computation time.

Therefore, the domain is discretized into $2 \times 2 \times 193$ grid points. Based on the friction velocity $u_\tau^* = \sqrt{\tau_b^*/\rho}$ (where τ_b is the bottom shear stress), the Reynolds number has a value of $\mathrm{Re}_\tau = u_\tau^* H^*/\nu = 180$. With a constant time step $\Delta t = 0.01$, the simulation starts from rest and terminates at $t = 2000$ when the flow, driven by a vertically uniform pressure gradient $\mathbf{S} = \begin{bmatrix} 1 & 0 & 0 \end{bmatrix}$, reaches a steady state. The analysis of difference between the numerical and analytical solution is shown in Figure 3, where the normalized root-mean-square error (NRMSE) is defined as

$$\mathrm{NRMSE}\left(t_n\right) = \frac{\sqrt{\frac{\sum_{l=0}^{N_3-1}\left[u_1\left(x_{3l};t_n\right) - u_{1a}\left(x_{3l};t_n\right)\right]^2}{N_3}}}{\max\left(\left|u_{1a}\left(x_{3l};t_n\right)\right|\right)}. \tag{37}$$

In above equation, u_1 denotes the numerically computed result, t_n denotes the evolution time at the n^{th} time step, and x_{3l} denotes the position of the l^{th} grid point in vertical direction. Demonstrated in Figure 3, the relative error is already very small in the very beginning of the simulation, and the error decreases rapidly from the order of 10^{-6} to 10^{-11} in 500 time units. This small equilibrium value of error is maintained to the end of the simulation, indicating that our numerical system has a stable spatial discretization in vertical direction and it is capable of simulating transient laminar flow with high accuracy.

Since the pioneering work of Kim et al. (1987), the direct numerical simulation of fully developed turbulent channel flow at $\mathrm{Re}_\tau = 180$ becomes the standard benchmark test for a DNS code. Same as the configuration in Moser et al. (1999), the domain size is set to be $4\pi H \times 4\pi H/3 \times 2H$ and we implement $256 \times 192 \times 193$ grid points in the streamwise, spanwise and vertical directions, respectively. Having a Reynolds number $\mathrm{Re}_\tau = 180$ and driven by the constant pressure gradient $\mathbf{S} = \begin{bmatrix} 1 & 0 & 0 \end{bmatrix}$, the flow is initialized with a mean current and divergence-free sinusoidal perturbations which are functions of x_3. The turbulence develops after several time units and the whole computation lasts for 120 units of time with a maximum Courant number of 0.25. After time- and plane-averaging over the last 100 time units, vertical profile of the streamwise velocity

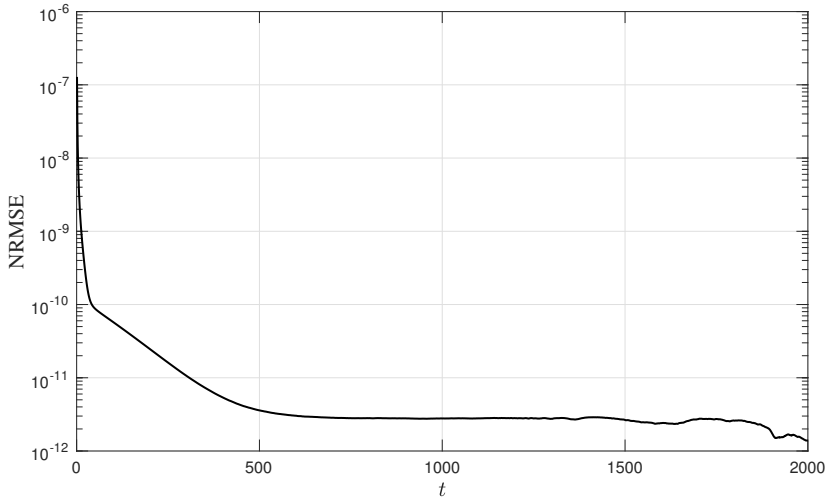

Figure 3. Normalized root-mean-square error analysis of the velocity profile for transient laminar channel flow under a constant pressure gradient at $\mathrm{Re}_\tau = 180$.

is shown in Figure 4. For better presentation, variables denoted by superscript '+' are non-dimensionalized with the viscous length scale ν/u_τ (thus in terms of the wall unit) and the friction velocity u_τ. In this report, the Von Karman constant has a typical value of $\kappa = 0.41$ and Figure 4 illustrates the very good approximation of the entire streamwise velocity profile using the law of the wall. To quantify turbulent fluctuation, the turbulence intensity for each fluctuating velocity component is computed and a comparison is presented in Figure 5. The present simulation results agree very well with the DNS results reported by Moser et al. (1999), demonstrating that the present numerical scheme is capable of simulating turbulent channel flow at low Reynolds number.

4.2. Statistically Steady Open Channel Flow

As mentioned in Section 2.1, for many sediment transport applications, it is more desirable to have a free-slip surface rather than a no-slip wall at top of the computational domain. Another commonly encountered example is the simulation of wave boundary layer with a superimposed mean current. In present work, the simulation of a fully turbulent open channel flow at $\mathrm{Re}_\tau = u_\tau^* L_3^*/\nu = 180$

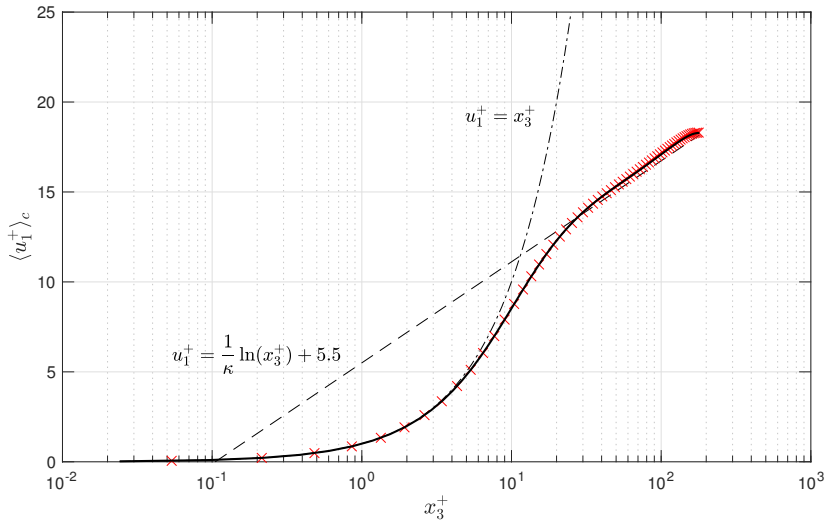

Figure 4. Ensemble-averaged streamwise velocity profile of the turbulent channel flow at $\mathrm{Re}_\tau = 180$. The black line represents the result from the present simulation, while the red crosses are corresponding model results reported by Moser et al. (1999).

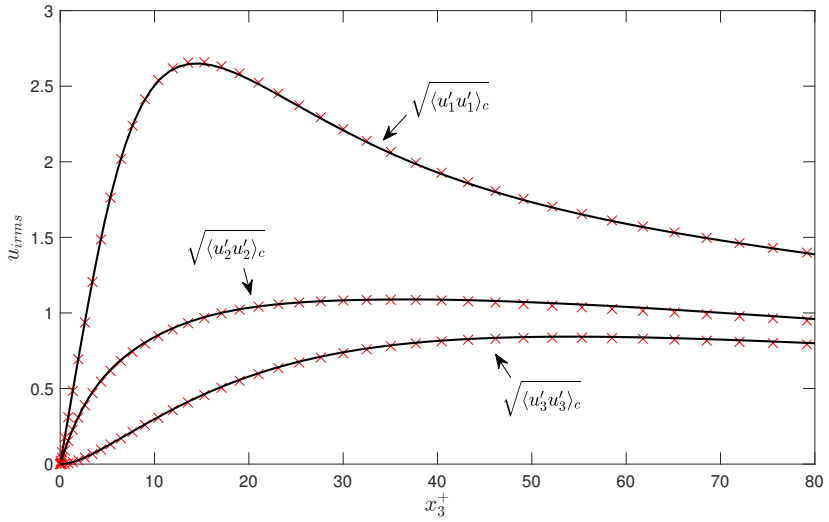

Figure 5. Turbulence intensity for each fluctuating velocity component of the turbulent channel flow at $\mathrm{Re}_\tau = 180$. The black lines represent the results from current simulation, while the red crosses are corresponding model results reported by Moser et al. (1999).

is also carried out where the domain height L_3^* (total channel height) is taken to be the characteristic length scale. In this case, the domain has a size of $4\pi L_3 \times 3\pi L_3/2 \times L_3$ while the number of grid point is specified as $128 \times 128 \times 129$ in the three directions, correspondingly. Still driven by a constant pressure gradient $\mathbf{S} = \begin{bmatrix} 1 & 0 & 0 \end{bmatrix}$, the streamwise flow becomes fully turbulent quickly from a initially perturbed state. After establishing a statistically steady state, turbulence statistics are computed based on the data of last 150 time units. The ensemble-averaged (time and plane averaged) streamwise velocity profile is rescaled in wall units and plotted in Figure 6(a). As the figure shows, the resulting velocity profile follows the analytical expression very well in both the viscous sublayer ($x_3^+ < 5$) and the log-law region ($x_3^+ > 30$). In the buffer layer ($5 < x_3^+ < 30$), the two computed velocity profiles are close to each other and shows a transitional feature connecting the viscous sublayer and the log-law region smoothly. The computed turbulence intensities are presented in Figure 6(b). Compared to an earlier DNS results reported in Handler et al. (1999), a very good agreement is found which indicates that the present model is capable for the numerical simulations of fully turbulent open channel flow at a low Reynolds number.

We further verify the model's capability in simulating dilute fine sediment transport in the turbulent open channel flow at $\mathrm{Re}_\tau = 180$. We keep all the settings for carrier flow the same and the critical bottom shear stress of erosion in this case is set to be $\tau_c = 0.99$ which is close to but slightly smaller than the analytical mean bottom shear stress ($\langle \tau_b \rangle_c = 1$). The resulting sediment suspension has a time and domain averaged concentration $\overline{\Phi} = \langle \overline{\phi} \rangle_{123} = 4.85 \times 10^{-5}$ (Figure 7(b)) which is dilute enough such that the turbulence damping effects caused by the sediment-induced density stratification is negligible. After taking the time and plane-averaging on both sides of Equation (5), the following budget equation of sediment flux in vertical direction is derived (Nelson and Fringer (2018))

$$\langle u_3' \phi' \rangle_c - w \langle \phi \rangle_c - \frac{1}{\mathrm{ReSc}} \frac{\partial \langle \phi \rangle_c}{\partial x_3} = 0, \tag{38}$$

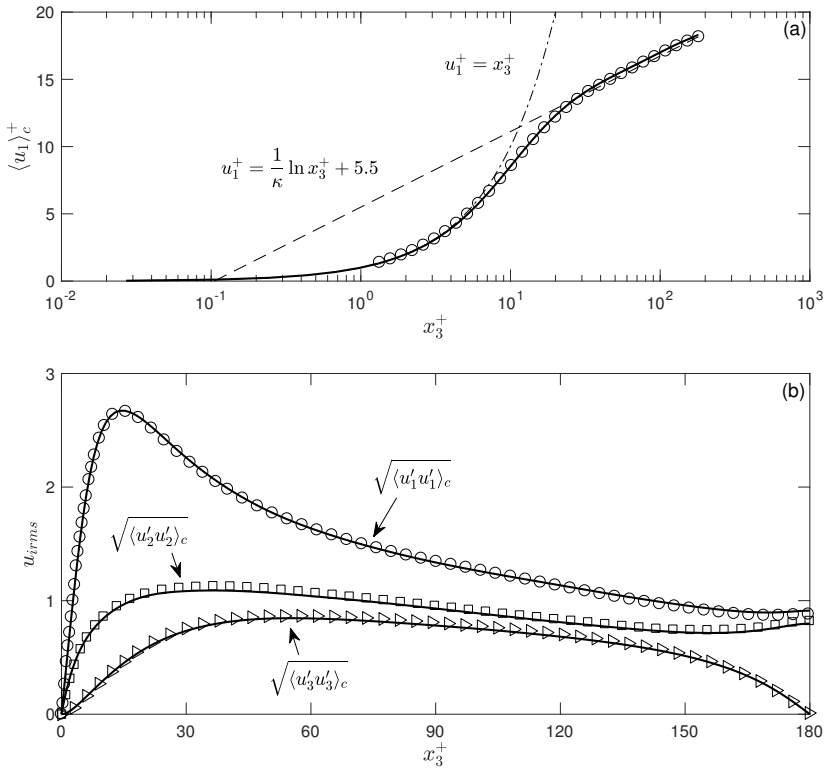

Figure 6. (a) Ensemble-averaged profile of the streamwise velocity; (b) Turbulence intensities in the three directions of the turbulent open channel flow at $\mathrm{Re}_\tau = 180$. The black lines represent the results from the present simulation, while symbols are the corresponding DNS results reported by Handler et al. (1999).

where the three components on left-hand side are the turbulent flux, the settling flux, and the diffusive sediment flux, respectively. Shown in Figure 7(a), the upward diffusive flux roughly balances the downward settling flux in the near-bed region (in the viscous sublayer). In the buffer layer ($x_3^+ < 30$), the turbulent flux becomes larger as the height increases and it eventually takes over the role of diffusive flux in this budget at $x_3^+ \approx 30$. In the log-law region, the upward turbulent flux dominates and it is the only term that balance with the downward settling flux, which results in the well-known Rouse profile for vertical

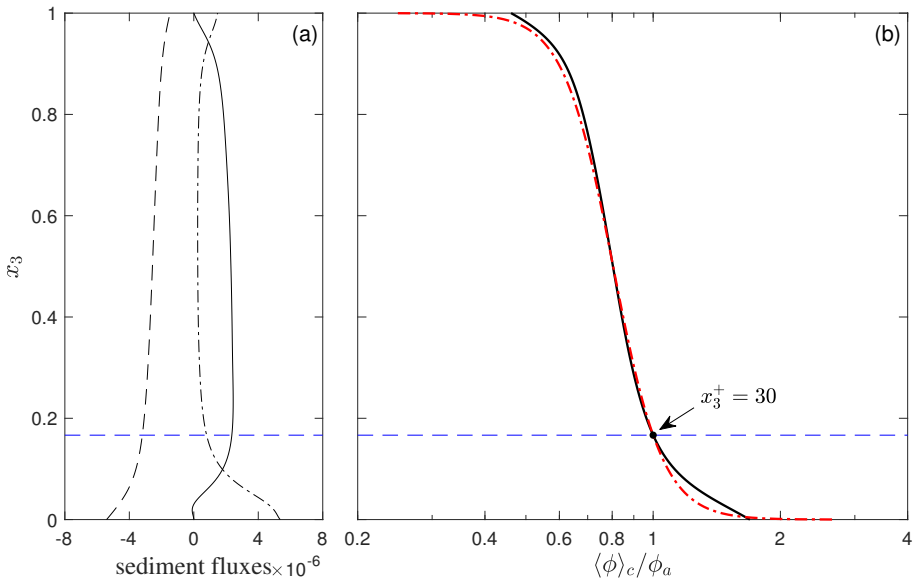

Figure 7. Sediment flux budget and concentration distribution of dilute fine sediment transport in the turbulent open channel flow at $\mathrm{Re}_\tau = 180$. (a) Three components in the sediment flux budget: the turbulent (solid line), the diffusive (dash-dot line), and the settling (dashed line) fluxes; (b) Ensemble-averaged profile of the volumetric concentration (solid line) with the matched theoretical Rouse profile (dash-dot line) in the log-law region.

distribution of sediment concentration (Rouse (1937))

$$\phi_R = \phi_a \left(\frac{1 - x_3}{x_3} \frac{a}{1 - a} \right)^{\mathrm{Z}}, \tag{39}$$

where ϕ_a is the reference concentration at a specific height $x_3 = a$, and $\mathrm{Z} = w/\kappa u_\tau = 0.14$ is the Rouse number. Following Nelson and Fringer (2018), the reference height is chosen to be the top of the buffer layer ($x_3^+ = 30$) where the reference concentration $\phi_a = 5.75 \times 10^{-5}$ in current simulation. Figure 7(b) shows a good fit of the theoretical Rouse profile with the computed concentration distribution in the log-law region. This also confirms that the turbulence damping effects from suspended sediment are negligible.

4.3. Statistically Steady Oscillatory Flow

In addition to the statistically steady channel (Section 4.1) and open channel (Section 4.2) flow, the scenario of oscillatory flow is also of interest for many

coastal bottom boundary layer applications. Similar to the transient laminar channel flow discussed previously, the transient laminar oscillatory flow is another good example of time-dependent flow problem amenable to exact mathematical analysis and the analytical solution which reads (Duarte et al. (2008); Langlois and Deville (2014))

$$u_{1a} = \mathrm{Re}\left\{ i \left[\frac{\cosh\left(\sqrt{i}\alpha x_3\right)}{\cosh\left(\sqrt{i}\alpha\right)} - 1 \right] \exp\left(it\right) \right\}, \tag{40}$$

where $i^2 = -1$ and $\alpha = \sqrt{\mathrm{Re}}$. In this laminar flow, an oscillatory pressure gradient $\mathbf{S} = \begin{bmatrix} \cos t & 0 & 0 \end{bmatrix}$ with a period of $T_w = 2\pi$ is applied in streamwise direction. Taking the amplitude of free stream velocity U_w^* and half domain height H^* as the velocity and length scales, the resulting Reynolds number has a value of $\mathrm{Re} = 180$. We use the same configuration used for the laminar channel flow (Section 4.1) and thus the domain size and grid number are of $4\pi H \times 4\pi H/3 \times 2H$ and $2 \times 2 \times 129$, respectively. Initialized with the analytical velocity profile at $t = 0$ based on Equation (40), the simulation terminates at $t = 8T_w$ with a time step $\Delta t = T_w/12000$. Still, a very small relative error around 10^{-9} to 10^{-8} is found from the analysis of NRMSE (Equation (37)), though it is relatively larger than the one found in Figure 3 which is about 10^{-11}. The reason for this difference is caused by the discretization of a continuous time-varying driving force. However, we still can conclude that the numerical treatment of the time-dependent force in Equation (2) in our modeling system is sufficiently accurate.

The turbulent Stokes boundary layer (SBL) is also a classical flow for DNS benchmarking. Unlike its steady counterpart illustrated in Section 4.2, the SBL can be intermittently turbulent, having a transition between laminar and turbulent states (Ozdemir et al. (2014)). Hence, it attracts many researchers' attention, particularly for testing the capability of a DNS code. In this study, we carry out a simulation at Stokes Reynolds number $\mathrm{Re}_\Delta = U_w^*\Delta^*/\nu = 1000$. This is equivalent to an energetic field condition with a free-stream velocity amplitude $U_w^* = 0.56\,\mathrm{m/s}$ and wave period $T_w^* = 10\,\mathrm{s}$ in which WSGFs were

observed (Traykovski et al. (2000)). By defining $\omega^* = 2\pi/T^*$ as the angular frequency of wave, the thickness of SBL is $\Delta^* = \sqrt{2\nu/\omega^*} = 1.78\,\mathrm{mm}$. For the configuration of numerical model, the domain has a size of $60\Delta \times 30\Delta \times 60\Delta$ and the number of grid is specified as $192 \times 192 \times 193$ in the three directions, respectively. The time step is chosen to be $\Delta t = \pi/5760$ and a time-dependent oscillatory pressure gradient force $\mathbf{S} = \begin{bmatrix} 2/\mathrm{Re}_\Delta \cos\left(2t/\mathrm{Re}_\Delta\right) & 0 & 0 \end{bmatrix}$ is applied in the streamwise direction to drive the boundary layer flow. The plane- and phase-averaged streamwise velocity profiles for six different phases in a wave period is shown in Figure 8, where the phase function is defined as $\varphi = \omega t$. The agreement with previous DNS results of Cheng et al. (2015c) is excellent. Comparing with the corresponding laminar solutions, we can see that at the intermittently turbulent condition with $\mathrm{Re}_\Delta = 1000$, the oscillatory boundary layer thickness becomes significantly larger.

Fine sediment transport in oscillatory bottom boundary layer is one of our key objectives to develop this numerical model. Applying the same Eulerian-Eulerian framework (Equations (2) and (5)), the regimes of sediment transport in an oscillatory channel show the correlation with turbulence modulation due to particle-turbulence interaction (Cantero et al. (2014); Cantero-Chinchilla et al. (2015)), which is controlled by a specified constant sediment availability (Ozdemir et al. (2010)). Relying on the critical bottom shear stress and settling velocity of sediment, variable sediment availability demonstrates the existence of three transport modes of fine sediment in the wave boundary layer due to different degrees of sediment-induced density stratification (Cheng et al. (2015b)). Here, we select the critical bottom shear stress and the settling velocity similar to the configuration of Case 2 reported in Cheng et al. (2015b), in which a two-layer-like transport mode of fine sediment was obtained. In this simulation, the erodible bed has a critical bottom shear stress of erosion of $\tau_c^* = 0.025\,\mathrm{Pa}$ and an empirical erosion rate of $m_e^* = 3 \times 10^{-7}\,\mathrm{m/s}$. With the specified settling velocity, these bed erodibility parameters allow for a sediment load close to the carrying capacity of flow as discussed in Cheng et al. (2015b). The oscillatory flow is driven by the same parameters used in the Stokes boundary layer study

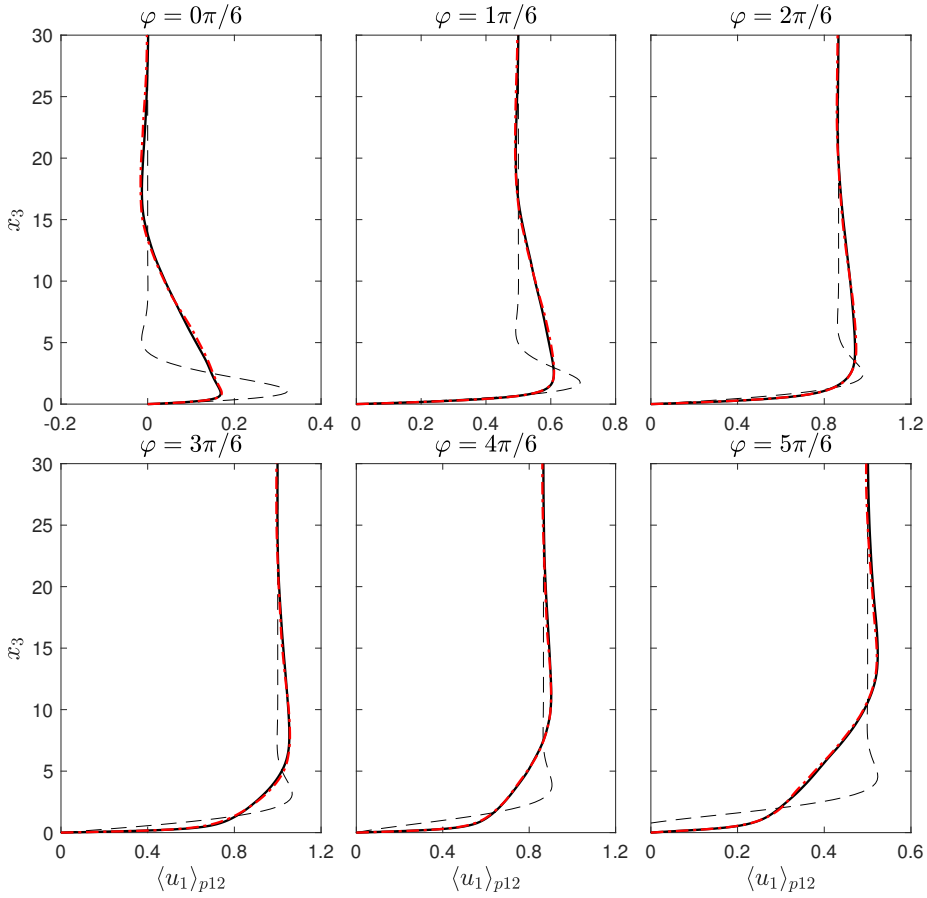

Figure 8. Phase-averaged streamwise velocity profiles at six phases (phase function $\varphi = 0\pi/6$ to $5\pi/6$) of the turbulent oscillatory flow at $\mathrm{Re}_\Delta = 1000$. Black dashed lines are corresponding laminar solutions, red dash-dot lines are numerical results of Cheng et al. (2015c), and black solid lines are present simulation results

discussed above. Based on the Stokes boundary-layer thickness Δ^*, the computational domain has a size of $60\times30\times60$ which is discretized with $256\times192\times193$ grid points in the two horizontal and bed-normal directions, respectively.

Data analysis of 20 wave periods is performed after the flow reaches a quasi-steady state. Transitional features of the flow is examined first through the visualization of coherent turbulent structures during the acceleration (Figure 9) and deceleration (Figure 10) instants. In this study, we use the method of

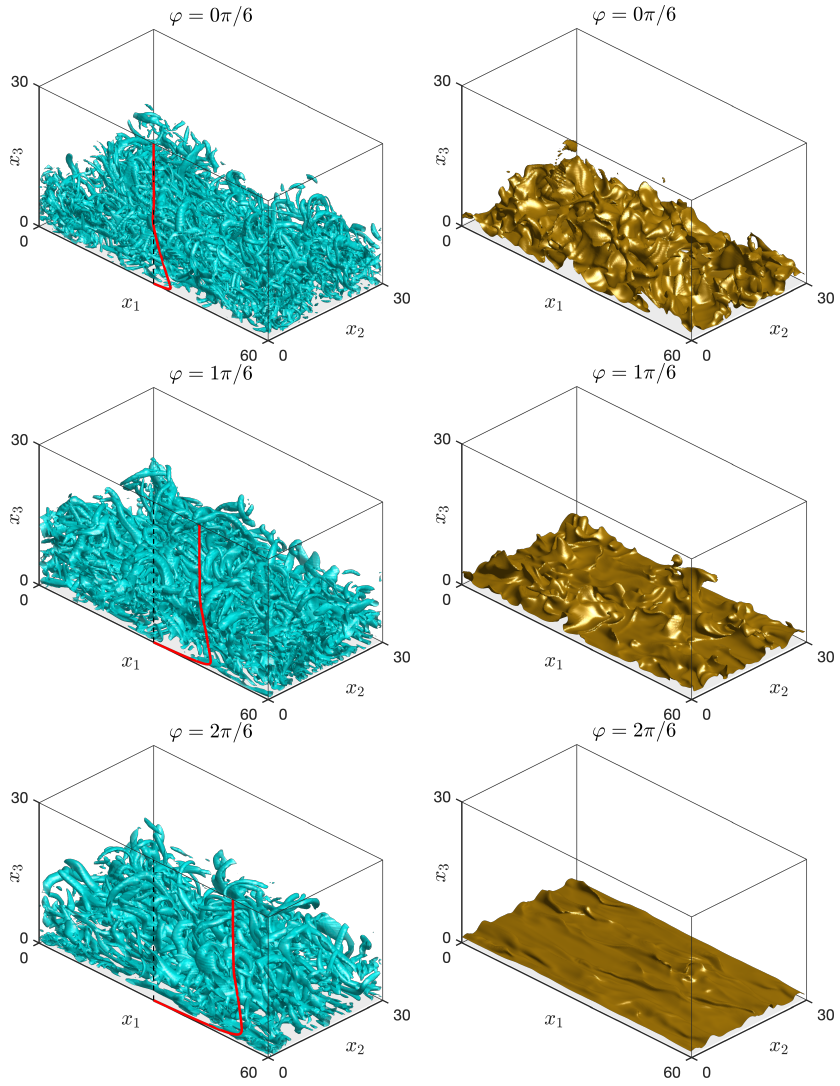

Figure 9. Coherent turbulent structures of flow (left) and corresponding isosurfaces of near-bed sediment concentration (right) at wave phases $\varphi = 0\pi/6, 1\pi/6$ and $2\pi/6$. The turbulent coherent structures are visualized using the swirling strength (λ_{ci}) where the contour levels are set to be 10% of the corresponding maximum values where $\max(\lambda_{ci}) = 13.75$, 7.28 and 5.85 for the three phases, respectively. Red lines in those plots denote the plan-averaged velocity in the streamwise direction. The contour levels of sediment concentration are chosen to be the averaged value at position $x_3 = 1.5$ which are 7.14×10^{-3}, 7.01×10^{-3} and 7.22×10^{-3}, correspondingly.

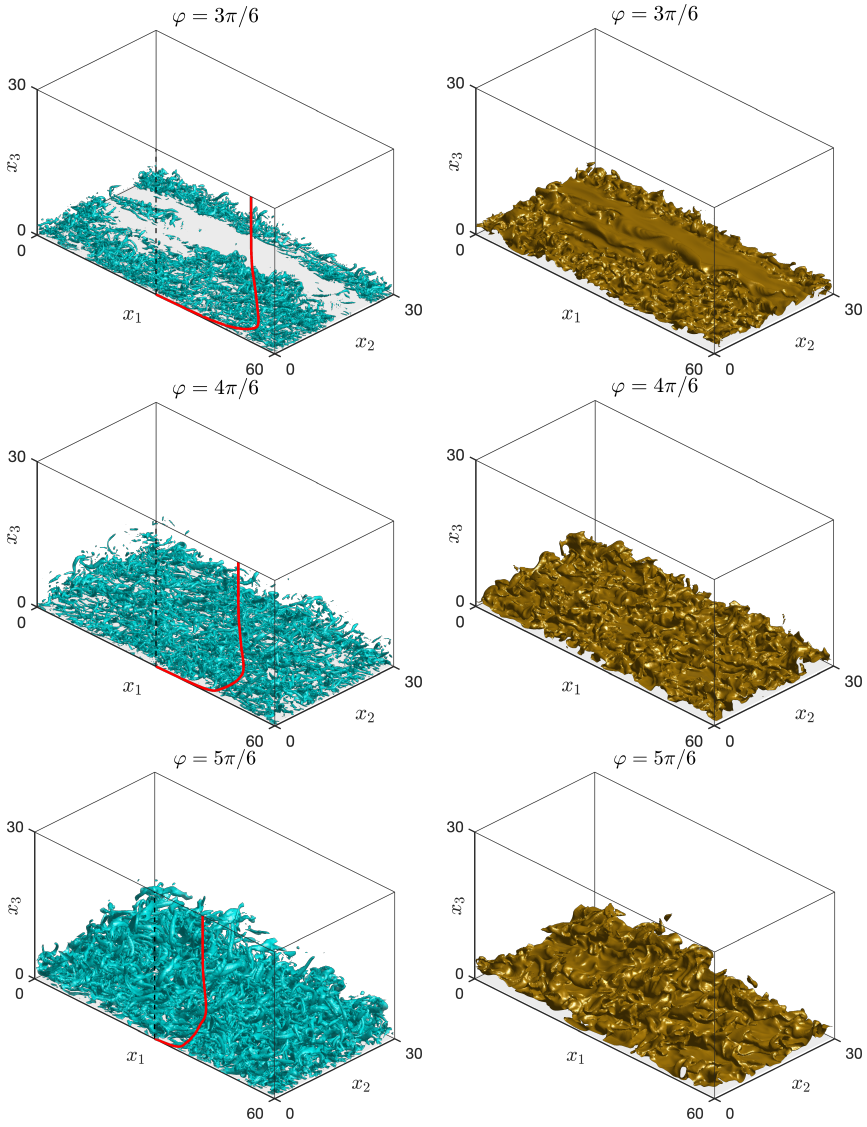

Figure 10. Continue of Figure 9 but at wave phases $\varphi = 3\pi/6, 4\pi/6$ and $5\pi/6$. For the three phases, the maximum swirling strength are $\max(\lambda_{ci}) = 88.21$, 59.16 and 23.61, while the contour levels of sediment concentration are 7.63×10^{-3}, 7.73×10^{-3} and 7.48×10^{-3}, correspondingly.

swirling strength λ_{ci} (Zhang et al. (2018)) to visualize turbulent coherent structures. Note that the value represented by the iso-surface of λ_{ci} in each phase is determined as 10% of the maximum value in the domain. We observe that these maximum values during the acceleration stage are generally lower than those of deceleration stage (see the captions of Figures 9 and 10), which is consistent with the temporal evolution of the bottom shear stress shown in Figure 12(b). At $\varphi = 0$ and $\pi/6$, we observe weaker turbulent coherent structures with larger sizes elevated from the bed and as it is demonstrated in Figure 11, these are mostly leftover turbulent features generated in the previous wave phase. On the other hand, more intense turbulent coherent structures at $\varphi = 3\pi/6$ and $4\pi/6$ are observed close to the bed. Compared to those observations during the acceleration phase, these coherent structures are of smaller size and very densely populated. Interestingly, the iso-surface of λ_{ci} at $\varphi = 2\pi/6$ shows very high spatial variability. A part of the domain has almost no turbulent coherent structures with λ_{ci} exceeding the corresponding iso-value compared to other portion of the domain. Due to the fine sediment assumption (see Section 2.2.1), the iso-surfaces of sediment concentration generally respond directly to the coherent turbulent structures and the intensity of turbulence throughout the entire wave cycle.

Figure 11 presents the turbulence-averaged (via plane- and phase-averaging) profiles of the streamwise flow velocity, the suspended sediment concentration, and the turbulence kinetic energy (TKE, $\langle k \rangle_{p12} = 0.5\langle u_i' u_i' \rangle_{p12}$) at phase of the lowest ($\varphi = \pi/6$) and the highest ($\varphi = 3\pi/6$) turbulence intensity. Although the magnitude of TKE increases by about ten times from $\varphi = \pi/6$ to $\varphi = 3\pi/6$, the sediment concentration only increases slightly due to relatively low settling velocity. More importantly, both concentration profiles show the feature of a sharp negative sediment concentration gradient, called the lutocline, located around $x_3 = 15.5$. As discussed in previous studies Cheng et al. (2015b); Ozdemir et al. (2010), the formation of lutocline is a prominent feature resulting from the sediment-induced stable density stratification which attenuates fluid turbulence. Thus, a majority of suspended sediments is confined below the luto-

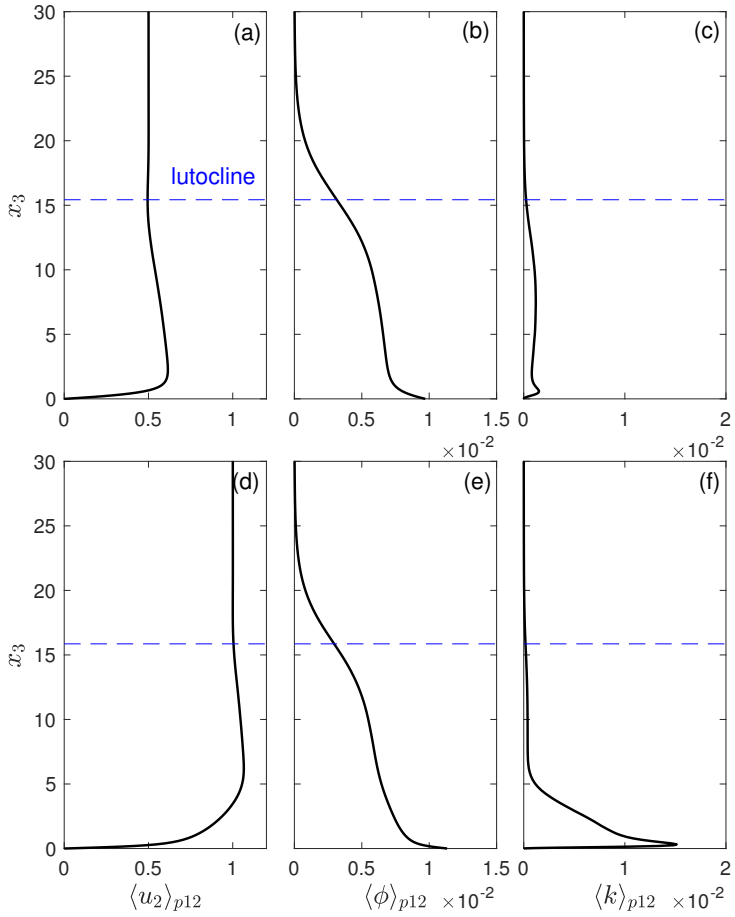

Figure 11. Phase- and plane-averaged (a,d) streamwise velocity; (b,e) volumetric concentration of sediment; (c,f) turbulence kinetic energy of flow. Subplots in the first and second row represent results at wave phase $\varphi = 1\pi/6$ and $3\pi/6$, respectively.

cline and a remarkable amount of persistent sediment load is suspended between $x_3 = 0$ and $x_3 = 16$ throughout the entire wave period.

Figure 12 shows the temporal evolution of the free-stream velocity, the phase-averaged magnitude of bottom shear stress $\left|\langle \tau_b^* \rangle_{p12}\right|$, and phase-domain-averaged sediment concentration. Demonstrated in Figure 12(b), there is an almost persistent erosion of sediment (upward erosional flux) because the plane-averaged bottom shear stress magnitude is greater than the critical shear stress

of erosion (0.025 Pa) nearly the entire wave cycle. Moreover, these bottom shear stress is different from the corresponding laminar solution. During the first acceleration stage between $\varphi = 0$ and $2\pi/6$, the bottom shear stress more or less follows the laminar solution, and the well-known phase lead of $\pi/4$ (Cheng et al. (2015b)) is evident. Soon after $\varphi = 2\pi/6$, the bottom shear stresses increase rapidly to reach their peak values of about 0.85 Pa at around the wave crest of $\varphi = 3\pi/6$. During the corresponding deceleration stage between $\varphi = 3\pi/6$ and $6\pi/6$, the bottom shear stresses decrease to zero before the flow reversal. These features are distinctly different from the laminar solution. Figure 12(c) confirms that the turbulent suspension dominates the settling effect of sediment and thus the sediments can be almost constantly suspended in the computational domain without significant temporal change (note the scale in the vertical axis). How-

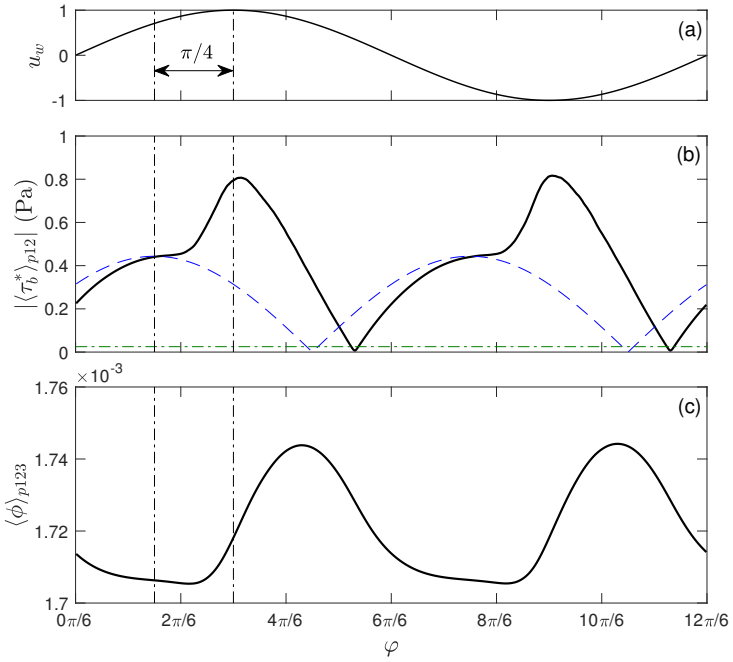

Figure 12. Phase evolution of (a) free-stream velocity; (b) amplitude of bottom shear stress; (c) domain-averaged volumetric concentration of sediment. The blue dashed line in subplot (b) is the corresponding laminar solution, while the green dash-dot line represents the critical bottom shear stress.

ever, a notable increase of sediment concentration still can be observed around the burst of bottom shear stress.

5. Conclusion and Future Work

A novel numerical modeling system for simulating bottom boundary layer and fine sediment transport is developed. Aiming at modeling fine sediment transport in water in which the Stokes number is often small, the model utilizes the equilibrium Eulerian approximation instead of the Eulerian two-phase flow for fluid-particle system. The mathematical formulation is numerically solved by a pseudo-spectral scheme written in `C++`. The numerical framework functioned by the Massage Passage Interface is suitable for a distributed memory computer system and a good scalability is obtained.

The numerical model is benchmarked by simulating statistically steady (open) channel and oscillatory flows in both laminar and turbulent situations. The numerical modeling framework is currently applied to study the dynamics of wave-supported gravity-driven sediment flows over flat bed. In near future, the numerical model will be extended in the same framework established in this report for modeling turbulent flow and fine sediment transport over bedforms, and mixed sediment transport condition with multiple classes of sediment.

References

Arakawa, A., Lamb, V.R., 1981. A Potential Enstrophy and Energy Conserving Scheme for the Shallow Water Equations. Monthly Weather Review 109, 18–36. URL: https://doi.org/10.1175/1520-0493(1981)109{%}3C0018:APEAEC{%}3E2.0.CO;2, doi:10.1175/1520-0493(1981)109<0018:APEAEC>2.0.CO;2.

Baj, P., Bruce, P.J.K., Buxton, O.R.H., 2015. The triple decomposition of a fluctuating velocity field in a multiscale flow. Physics of Fluids 27, 075104. URL: http://aip.scitation.org/doi/10.1063/1.4923744, doi:10.1063/1.4923744.

Balachandar, S., Eaton, J.K., 2010. Turbulent Dispersed Multiphase Flow. Annual Review of Fluid Mechanics 42, 111–133. URL: http://www.annualreviews.org/doi/10.1146/annurev.fluid.010908.165243, doi:10.1146/annurev.fluid.010908.165243.

Cantero, M.I., Balachandar, S., Cantelli, A., Parker, G., 2014. A simplified approach to address turbulence modulation in turbidity currents as a response to slope breaks and loss of lateral confinement. Environmental Fluid Mechanics 14, 371–385. URL: http://link.springer.com/10.1007/s10652-013-9302-7, doi:10.1007/s10652-013-9302-7.

Cantero, M.I., Balachandar, S., Cantelli, A., Pirmez, C., Parker, G., 2009a. Turbidity current with a roof: Direct numerical simulation of self-stratified turbulent channel flow driven by suspended sediment. Journal of Geophysical Research: Oceans 114, C03008. URL: http://doi.wiley.com/10.1029/2008JC004978, doi:10.1029/2008JC004978.

Cantero, M.I., Balachandar, S., García, M.H., 2008. An EulerianEulerian model for gravity currents driven by inertial particles. International Journal of Multiphase Flow 34, 484–501. URL: https://www.sciencedirect.com/science/article/pii/S0301932207001723, doi:10.1016/J.IJMULTIPHASEFLOW.2007.09.006.

Cantero, M.I., Balachandar, S., Parker, G., 2009b. Direct numerical simulation of stratification effects in a sediment-laden turbulent channel flow. Journal of Turbulence 10, N27. URL: http://www.tandfonline.com/doi/abs/10.1080/14685240903159197, doi:10.1080/14685240903159197.

Cantero-Chinchilla, F.N., Dey, S., Castro-Orgaz, O., Ali, S.Z., 2015. Hydrodynamic analysis of fully developed turbidity currents over plane beds based on self-preserving velocity and concentration distributions. Journal of Geophysical Research: Earth Surface 120, 2176–2199. URL: http://doi.wiley.com/10.1002/2015JF003685, doi:10.1002/2015JF003685.

Canuto, C., Hussaini, M.Y., Quarteroni, A., Zang, T.A., 1988. Spectral Methods in Fluid Dynamics. Springer Berlin Heidelberg, Berlin, Heidelberg. URL: http://link.springer.com/10.1007/978-3-642-84108-8, doi:10.1007/978-3-642-84108-8.

Cheng, Z., Yu, X., Hsu, T.J., Balachandar, S., 2015a. A numerical investigation of fine sediment resuspension in the wave boundary layer — Uncertainties in particle inertia and hindered settling. Computers & Geosciences 83, 176–192. URL: https://www.sciencedirect.com/science/article/pii/S0098300415300170, doi:10.1016/J.CAGEO.2015.07.009.

Cheng, Z., Yu, X., Hsu, T.J., Ozdemir, C.E., Balachandar, S., 2015b. On the transport modes of fine sediment in the wave boundary layer due to resuspension/deposition: A turbulence-resolving numerical investigation. Journal of Geophysical Research: Oceans 120, 1918–1936. URL: http://doi.wiley.com/10.1002/2014JC010623, doi:10.1002/2014JC010623.

Cheng, Z., Yu, X., Ozdemir, C.E., Hsu, T.J., Balachandra, S.B., 2015c. A turbulence-resolving numerical model for fine sediment transport in the bottom boundary layer — finesed3d (version 1.0). URL: https://www.semanticscholar.org/paper/A-TURBULENCE-RESOLVING-NUMERICAL-MODEL-FOR-FINE-IN-Cheng-Xiao/d70ad71c4e9811486383c3029035354a62c8615c.

Chorin, A.J., 1968. Numerical solution of the Navier-Stokes equations. Mathematics of Computation 22, 745–745. URL: http://www.ams.org/jourcgi/jour-getitem?pii=S0025-5718-1968-0242392-2, doi:10.1090/S0025-5718-1968-0242392-2.

Cortese, T.A., Balachandar, S., 1995. High Performance Spectral Simulation of Turbulent Flows in Massively Parallel Machines With Distributed Memory. The International Journal of Supercomputer Applications and High Performance Computing 9, 187–204. URL: http://journals.sagepub.com/doi/10.1177/109434209500900302, doi:10.1177/109434209500900302.

Duarte, A., Miranda, A., Oliveira, P., 2008. Numerical and analytical modeling of unsteady viscoelastic flows: The start-up and pulsating test case problems. Journal of Non-Newtonian Fluid Mechanics 154, 153–169. URL: https://www.sciencedirect.com/science/article/pii/S037702570800092X, doi:10.1016/J.JNNFM.2008.04.009.

Ferry, J., Balachandar, S., 2001. A fast Eulerian method for disperse two-phase flow. International Journal of Multiphase Flow 27, 1199–1226. URL: https://www.sciencedirect.com/science/article/pii/S0301932200000690, doi:10.1016/S0301-9322(00)00069-0.

Ferry, J., Rani, S.L., Balachandar, S., 2003. A locally implicit improvement of the equilibrium Eulerian method. International Journal of Multiphase Flow 29, 869–891. URL: https://www.sciencedirect.com/science/article/pii/S0301932203000648, doi:10.1016/S0301-9322(03)00064-8.

Ge, M.w., Xu, C.x., Cui, G.x., 2010. Direct numerical simulation of flow in channel with time-dependent wall geometry. Applied Mathematics and Mechanics 31, 97–108. URL: http://link.springer.com/10.1007/s10483-010-0110-x, doi:10.1007/s10483-010-0110-x.

Hale, R.P., Ogston, A.S., 2015. In situ observations of wave-supported fluid-mud generation and deposition on an active continental margin. Journal of Geophysical Research: Earth Surface 120, 2357–2373. URL: http://doi.wiley.com/10.1002/2015JF003630, doi:10.1002/2015JF003630.

Handler, R.A., Saylor, J.R., Leighton, R.I., Rovelstad, A.L., 1999. Transport of a passive scalar at a shear-free boundary in fully developed turbulent open channel flow. Physics of Fluids 11, 2607. URL: https://aip.scitation.org/doi/abs/10.1063/1.870123, doi:10.1063/1.870123.

Hooshmand, A., Horner-Devine, A.R., Lamb, M.P., 2015. Structure of turbulence and sediment stratification in wave-supported mud layers. Journal of Geophysical Research: Oceans 120, 2430–2448. URL: http://doi.wiley.com/10.1002/2014JC010231, doi:10.1002/2014JC010231.

Kim, J., Moin, P., Moser, R., 1987. Turbulence statistics in fully developed channel flow at low Reynolds number. Journal of Fluid Mechanics 177, 133–166. URL: http://www.journals.cambridge.org/abstract{_}S0022112087000892, doi:10.1017/S0022112087000892.

Kwon, Y.S., Hutchins, N., Monty, J.P., 2016. On the use of the Reynolds decomposition in the intermittent region of turbulent boundary layers. Journal of Fluid Mechanics 794, 5–16. URL: http://www.journals.cambridge.org/abstract{_}S0022112016001610, doi:10.1017/jfm.2016.161.

Langlois, W.E., Deville, M.O., 2014. Slow Viscous Flow. Springer International Publishing, Cham. URL: http://link.springer.com/10.1007/978-3-319-03835-3, doi:10.1007/978-3-319-03835-3.

Meiburg, E., Kneller, B., 2010. Turbidity Currents and Their Deposits. Annual Review of Fluid Mechanics 42, 135–156. URL: http://www.annualreviews.org/doi/10.1146/annurev-fluid-121108-145618, doi:10.1146/annurev-fluid-121108-145618.

Moser, R.D., Kim, J., Mansour, N.N., 1999. Direct numerical simulation of turbulent channel flow up to Reτ=590. Physics of Fluids 11, 943–945. URL: http://aip.scitation.org/doi/10.1063/1.869966, doi:10.1063/1.869966.

Nelson, K.S., Fringer, O.B., 2018. Sediment Dynamics in Wind Wave-Dominated Shallow-Water Environments. Journal of Geophysical Research: Oceans URL: http://doi.wiley.com/10.1029/2018JC013894, doi:10.1029/2018JC013894.

Ozdemir, C.E., Hsu, T.J., Balachandar, S., 2010. A numerical investigation of fine particle laden flow in an oscillatory channel: the role of particle-induced density stratification. Journal of Fluid Mechanics 665, 1–45. URL: www.journals.cambridge.org/abstract{_}S0022112010003769, doi:10.1017/S0022112010003769.

Ozdemir, C.E., Hsu, T.J., Balachandar, S., 2014. Direct numerical simulations of transition and turbulence in smooth-walled Stokes boundary layer. Physics of Fluids 26, 045108. URL: http://aip.scitation.org/doi/10.1063/1.4871020, doi:10.1063/1.4871020.

Parker, G., Fukushima, Y., Pantin, H.M., 1986. Self-accelerating turbidity currents. Journal of Fluid Mechanics 171, 145. URL: http://www.journals.cambridge.org/abstract{_}S0022112086001404, doi:10.1017/S0022112086001404.

Pekurovsky, D., 2012. P3DFFT: A Framework for Parallel Computations of Fourier Transforms in Three Dimensions. SIAM Journal on Scientific Computing 34, C192—-C209. URL: http://epubs.siam.org/doi/10.1137/11082748X, doi:10.1137/11082748X.

Peyret, R., 2002. Spectral Methods for Incompressible Viscous Flow. Springer-Verlag New York. URL: http://www.springer.com/gp/book/9780387952215, doi:10.1007/978-1-4757-6557-1.

Remmler, S., Fruman, M.D., Hickel, S., 2013. Direct numerical simulation of a breaking inertiagravity wave. Journal of Fluid Mechanics 722, 424–436. URL: http://www.journals.cambridge.org/abstract{_}S0022112013001080, doi:10.1017/jfm.2013.108.

Reynolds, W.C., Hussain, A.K.M.F., 1972. The mechanics of an organized wave in turbulent shear flow. Part 3. Theoretical models and comparisons with experiments. Journal of Fluid Mechanics 54, 263. URL: http://www.journals.cambridge.org/abstract{_}S0022112072000679, doi:10.1017/S0022112072000679.

Rouse, H., 1937. Modern Conceptions of the Mechanics or Fluid Turbulence. Transactions of the American Society of Civil Engineers 102, 463–505. URL: https://cedb.asce.org/CEDBsearch/record.jsp?dockey=0288088.

Sanderson, C., Curtin, R., 2016. Armadillo: a template-based C++ library for linear algebra. Journal of Open Source Software 1, 26. URL: https://joss.theoj.org/papers/4d6506e46a96659b74f48b51ef92fa93, doi:10.21105/joss.00026.

Sanford, L.P., 2008. Modeling a dynamically varying mixed sediment bed with erosion, deposition, bioturbation, consolidation, and armoring. Computers & Geosciences 34, 1263–1283. URL: https://www.sciencedirect.com/science/article/pii/S0098300408000551?via{%}3Dihub, doi:10.1016/J.CAGEO.2008.02.011.

Sanford, L.P., Maa, J.P.Y., 2001. A unified erosion formulation for fine sediments. Marine Geology 179, 9–23. URL: https://www.sciencedirect.com/science/article/pii/S0025322701002018, doi:10.1016/S0025-3227(01)00201-8.

Shringarpure, M., Cantero, M.I., Balachandar, S., 2012. Dynamics of complete turbulence suppression in turbidity currents driven by monodisperse suspensions of sediment. Journal of Fluid Mechanics 712, 384–417. URL: http://www.journals.cambridge.org/abstract{_}S0022112012004272, doi:10.1017/jfm.2012.427.

Shringarpure, M.S., Cantero, M.I., Balachandar, S., 2014. Mechanisms of Complete Turbulence Suppression in Turbidity Currents Driven by Mono-Disperse and Bi-Disperse Suspensions of Sediment. The Journal of Computational Multiphase Flows 6, 221–245. URL: http://journals.sagepub.com/doi/10.1260/1757-482X.6.3.221, doi:10.1260/1757-482X.6.3.221.

Soulsby, R., Manning, A., Spearman, J., Whitehouse, R., 2013. Settling velocity and mass settling flux of flocculated estuarine sediments. Marine Geology 339, 1–12. URL: https://www.sciencedirect.com/science/article/abs/pii/S0025322713000388, doi:10.1016/J.MARGEO.2013.04.006.

Thorpe, S.A., 1987. Transitional phenomena and the development of turbulence in stratified fluids: A review. Journal of Geophysical Research 92,

5231. URL: http://doi.wiley.com/10.1029/JC092iC05p05231, doi:10.1029/JC092iC05p05231.

Traykovski, P., Geyer, W.R., Irish, J.D., Lynch, J.F., 2000. The role of wave-induced density-driven fluid mud flows for cross-shelf transport on the Eel River continental shelf. Continental Shelf Research 20, 2113–2140. URL: https://www.sciencedirect.com/science/article/pii/S0278434300000716, doi:10.1016/S0278-4343(00)00071-6.

Traykovski, P., Trowbridge, J., Kineke, G., 2015. Mechanisms of surface wave energy dissipation over a high-concentration sediment suspension. Journal of Geophysical Research: Oceans 120, 1638–1681. URL: http://doi.wiley.com/10.1002/2014JC010245, doi:10.1002/2014JC010245.

Traykovski, P., Wiberg, P.L., Geyer, W.R., 2007. Observations and modeling of wave-supported sediment gravity flows on the Po prodelta and comparison to prior observations from the Eel shelf. Continental Shelf Research 27, 375–399. URL: https://www.sciencedirect.com/science/article/pii/S0278434306003487, doi:10.1016/J.CSR.2005.07.008.

Trowbridge, J.H., Lentz, S.J., 2018. The Bottom Boundary Layer. Annual Review of Marine Science 10, 397–420. URL: http://www.annualreviews.org/doi/10.1146/annurev-marine-121916-063351, doi:10.1146/annurev-marine-121916-063351.

Williamson, J.H., 1980. Low-storage Runge-Kutta schemes. Journal of Computational Physics 35, 48–56. URL: https://www.sciencedirect.com/science/article/pii/0021999180900339, doi:10.1016/0021-9991(80)90033-9.

Winterwerp, J.C., van Kesteren, W.G.M., van Prooijen, B., Jacobs, W., 2012. A conceptual framework for shear flow-induced erosion of soft cohesive sediment beds. Journal of Geophysical Research: Oceans 117, n/a—-n/a. URL: http://doi.wiley.com/10.1029/2012JC008072, doi:10.1029/2012JC008072.

Xu, C., Subich, C., Stastna, M., 2016. Numerical simulations of shoaling internal solitary waves of elevation. Physics of Fluids 28, 076601. URL: http://aip.scitation.org/doi/10.1063/1.4958899, doi:10.1063/1.4958899.

Yang, D., Shen, L., 2011. Simulation of viscous flows with undulatory boundaries. Part I: Basic solver. Journal of Computational Physics 230, 5488–5509. URL: https://www.sciencedirect.com/science/article/pii/S0021999111001252, doi:10.1016/J.JCP.2011.02.036.

Zhang, Y., Liu, K., Xian, H., Du, X., 2018. A review of methods for vortex identification in hydroturbines. Renewable and Sustainable Energy Reviews 81, 1269–1285. URL: https://www.sciencedirect.com/science/article/pii/S1364032117306949, doi:10.1016/J.RSER.2017.05.058.

Zhao, L., Ouillon, R., Vowinckel, B., Meiburg, E., Kneller, B., He, Z., 2018. Transition of a Hyperpycnal Flow Into a Saline Turbidity Current Due to Differential Diffusivities. Geophysical Research Letters 45, 11,811–875,884. URL: http://doi.wiley.com/10.1029/2018GL080150, doi:10.1029/2018GL080150.